







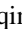



## Observation of non-Hermiticity-induced topological edge states in the continuum in a trimerized elastic lattice

Haiyan Fan <sup>1</sup>, He Gao <sup>1,\*</sup>, Shuwei An <sup>1</sup>, Zhongming Gu <sup>2</sup>, Yafeng Chen <sup>1,3</sup>, Sibao Huang <sup>1,2</sup>, Shanjun Liang <sup>4</sup>, Jie Zhu <sup>2,5</sup>, Tuo Liu <sup>6,7,†</sup> and Zhongqing Su <sup>1,‡</sup>

<sup>1</sup>Department of Mechanical Engineering, The Hong Kong Polytechnic University, Hung Hom, Kowloon, Hong Kong SAR, China

<sup>2</sup>Institute of Acoustics, School of Physics Science and Engineering, Tongji University, Shanghai 200092, China

<sup>3</sup>State Key Laboratory of Advanced Design and Manufacturing for Vehicle Body, Hunan University, Changsha 410082, China

<sup>4</sup>Division of Science, Engineering and Health Studies, College of Professional and Continuing Education, Hong Kong Polytechnic University, Hong Kong SAR, China

<sup>5</sup>Shanghai Research Institute for Intelligent Autonomous Systems, Tongji University, Shanghai 201210, China

<sup>6</sup>Key Laboratory of Noise and Vibration Research, Institute of Acoustics, Chinese Academy of Sciences, Beijing 100190, China

<sup>7</sup>State Key Laboratory of Acoustics, Institute of Acoustics, Chinese Academy of Sciences, Beijing 100190, China



(Received 16 May 2022; revised 27 September 2022; accepted 26 October 2022; published 14 November 2022)

Topologically protected localized states are commonly existent inside bulk band gaps with topological features, which, however, can be shifted to coexist with a continuous spectrum under particular coupling modulations, forming the so-called topological bound states in the continuum (BICs). These embedded topological states have so far been derived under the Hermitian assumptions that neglect the influence of nonconservative characteristics of classical wave systems on the topological properties. In this study, with a one-dimensional trimerized elastic lattice, we report the experimental demonstration of topological edge states in the continuum produced solely by non-Hermiticity, without additional coupling modulation. The trimerized elastic lattice is a chain of plates connected through thin beams, with the non-Hermiticity introduced by attaching constrained damping layers to particular sites in the chain assembly. We prove that appropriately tailored non-Hermitian modulation can induce topological edge states that appear in the bulk spectrum rather than exist in the band gap. Besides, the existence of such topological edge states is observed to be closely linked to the configurations of the lattice boundaries. This study affirms that non-Hermiticity can play an important role in creating topological BICs, gaining insight into the non-Hermitian topological physics and offering interesting avenues for exploring sophisticated non-Hermitian topological phenomena including higher-order topology in the continuum.

DOI: [10.1103/PhysRevB.106.L180302](https://doi.org/10.1103/PhysRevB.106.L180302)

### I. INTRODUCTION

Topological insulators, first emerged in condensed matter systems, are referred to the phases of matter that are characterized with insulating bulk and robust conducting edges [1,2]. The analogs of topological insulators in classical wave systems have been a solid ground, on which basis topological physics are investigated, discovering numerous intriguing phenomena, such as backscattering-free chiral edge modes associated with the quantum Hall-like effect [3–5] and localized edge (corner) modes due to the quantized bulk dipole (quadrupole) moments [6–10]. Most relevant studies in this area are based on the premise of Hermiticity, for its simplicity, with which the real eigenvalues and orthogonal eigenstates of their effective Hamiltonians ensure the well-defined topological invariants and bulk-edge correspondence [11,12]. Classical wave systems, however, are naturally non-Hermitian with loss and/or gain arising from the energy

exchange with the surrounding environment. Particularly, the intrinsic losses such as thermoviscous and viscoelastic effects, a major source of non-Hermiticity in realistic scenario, are usually considered as negative factors as they naturally lead to energy dissipation and inevitably increase the difficulty in experimental implementation. As a result, there is growing interest in exploring the interplay between the topology and non-Hermiticity so that the lossy nature can be properly exploited. To our delight, it has been demonstrated that the non-Hermiticity, *per se*, other than simply a perturbation to the topological systems, can be a nontrivial parameter to drive the topological phase transition [13–15]. This has motivated a cascade of theoretical explorations based on tight-binding Hamiltonians [16–21] and experimental demonstrations in electrical circuit [22], optical lattices [23,24], acoustic crystals [25–27], and elastic perturbative metamaterials [28] with suitably arranged loss and/or gain, which significantly extended the topological notions to non-Hermitian systems as well as their practical applications. In the majority of non-Hermitian topological systems, the topological properties are considered to exist in the band gaps which separate the spatially localized modes from the bulk continuous spectra of propagating waves. Yet, it is entirely possible that the localized topological states

\*Corresponding author: h.e.gao@connect.polyu.hk

†liutuo@mail.ioa.ac.cn

‡zhongqing.su@polyu.edu.hk

reside in bulk bands, behaving as the so-called bound states in the continuum (BICs) [29–32].

BICs are a class of spatially confined eigenmodes lying inside the continuous spectra. This notion has recently been extended to topological systems, which has inspired the theoretical exploration of topologically protected bound states against hybridization in electronic system [33], experimental investigation of subspace-induced embedded topological interface states in coupled one-dimensional (1D) acoustic chains [34], as well as the theoretical [35,36] and experimental efforts [37–39] in constructing in-band topological corner states known as higher-order topological BICs. The emergence of topological BICs can be attributed to the eigenfrequency shift of either bulk bands [34] or localized topological states [37] resulting from specific spatial variations in the coupling terms. It sheds light on novel topological physics, but relevant exploration has hitherto been restricted to the Hermitian regime. While a recent theory [40] based on the tight-binding model (TBM) suggests a possible direction to derive in-band topological states from parity-time (PT) symmetry with balanced gain and loss, the experimental observation of these non-Hermiticity-induced, in-band topological edge states remains unclear and challenging.

In this study, rather than resorting to balanced gain-loss configurations that is hard to achieve in practice, we develop a series of lossy and passive structures to experimentally demonstrate the non-Hermiticity-induced, in-band topological edge modes. The structures are 1D non-Hermitian trimerized models which consist of resonant plates and linking beams. Unlike the in-gap topological states that rely on alternating coupling strengths and Hermitian assumptions, the in-band topological states in the structures solely depend on the additionally introduced damping on particular lattice sites. As the additional damping (AD) is deliberately applied to the middle plate of the trimerized unit cell, two Dirac points are gradually lifted, creating two band gaps. Instead of appearing in the band gaps, the topological edge modes keep fixed within the continuous spectrum, behaving as BICs. The topological protection properties of the edge modes are indicated by the nonzero general Zak phases on the basis of the orthogonalized eigenstates. In experiment, we observe such non-Hermiticity-induced in-band topological edge modes by implementing the required non-Hermitian modulation with constrained damping layer treatments. This new non-Hermitian mechanism for achieving in-band topological edge modes is generally applicable to diverse systems (e.g., optical and acoustic systems, etc.) and is simple to realize.

## II. NON-HERMITIAN TRIMERIZED ELASTIC LATTICE MODEL

We focus on a trimerized elastic lattice consisting of resonant square plates that are mutually and weakly coupled via linking beams, with potential non-Hermitian modulation implemented by means of AD treatment, as depicted in Figs. 1(a) and 1(b). The lattice is made of aluminum alloy with a thickness of 1.46 mm and a lattice constant of  $a = 187.5$  mm. The sizes of the plates (with a hole of diameter  $D = 15$  mm in the center) and beams are  $40 \times 40$  mm<sup>2</sup> and  $22.5 \times 1.5$  mm<sup>2</sup>, respectively. The linking positions are

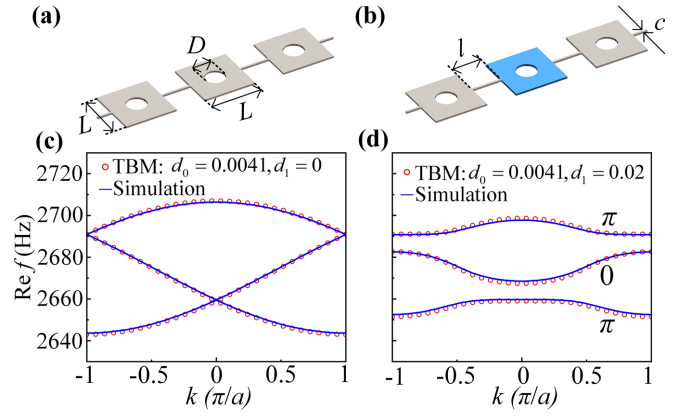


FIG. 1. Band diagrams of the trimerized elastic lattices in the absence and in the presence of the non-Hermitian modulation. (a),(b) Schematic diagrams of the unit cells for the trimerized lattices with only intrinsic material damping and with AD treatment (applied to the middle plate colored in blue), respectively.  $L = 40$  mm,  $D = 15$  mm,  $l = 22.5$  mm,  $c = 1.5$  mm. (c),(d) Calculated band diagrams corresponding to the unit cells in (a) and (b), respectively. The red circles denote the TBM results, and the blue solid lines denote the numerical results. The general Zak phases for the three bands in (d) are calculated to be  $\pi$ ,  $0$ ,  $\pi$ , respectively.

identical (located at the middle of the plate edge), leading to the identical nearest-neighbor coupling strength between two adjacent plates. Consequently, the band diagram of the trimerized unit cell in Fig. 1(a) is gapless, as presented in Fig. 1(c), in which the degeneracies emerge at the center and edge of the Brillouin zone (BZ). When AD treatment is introduced to the middle plate colored in blue in Fig. 1(b), both the degeneracies are lifted, giving rise to two complete band gaps, as shown in Fig. 1(d). In these elastic lattices, we only focus on the flexural modes.

The band diagrams of the unit cells illustrated in Figs. 1(a) and 1(b) can also be obtained by solving the eigenvalue problems of the tight binding  $k$ -space Hamiltonian matrices [41,42], which can be written as

$$H(k) = \begin{pmatrix} (1 - d_0 i)f_0 & \kappa & \kappa e^{-ika} \\ \kappa & [1 - (d_0 + d_1)i]f_0 & \kappa \\ \kappa e^{ika} & \kappa & (1 - d_0 i)f_0 \end{pmatrix} + \delta f \begin{pmatrix} 1 & 0 & 0 \\ 0 & 1 & 0 \\ 0 & 0 & 1 \end{pmatrix}, \quad (1)$$

where  $k$  is the wave number defined in the first BZ,  $f_0$  is the resonant frequency of the first nonrigid-body mode of an individual plate (in the absence of the linking beams),  $\kappa$  is the nearest-neighbor coupling strength,  $d_0$  describes the intrinsic material damping,  $d_1$  describes additionally introduced damping, and  $\delta f$  is the frequency deviation of the zero-energy edge modes from  $f_0$  due to the perturbation brought by the coupling beams [37]. By fitting the calculated band diagrams based on Eq. (1) [red dotted lines in Figs. 1(c) and 1(d)] to those obtained from the numerical simulation using COMSOL® Multiphysics [blue solid lines in Figs. 1(c) and 1(d)], we obtain the values of tight-binding parameters as  $f_0 = 2640$  Hz,  $\kappa = 16$  Hz,  $d_0 = 0.0041$ ,  $d_1 = 0.02$ , and  $\delta f = 36$  Hz. The match

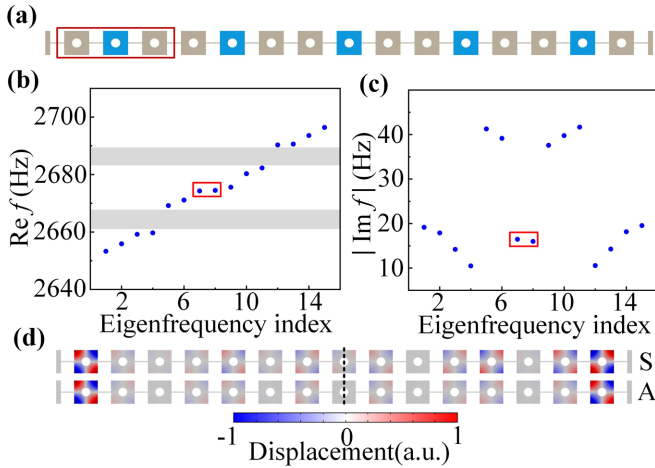


FIG. 2. Topological edge states in the continuum for a finite-sized chain assembly with 15 resonators. (a) Schematic of the chain composed of five unit cells. The red box indicates the trimerized nontrivial unit cell. The intrinsic material damping of the whole structure is considered, while the additional damping is only added to the sites colored in blue. Simulated real parts (b) and imaginary parts (c) of the complex eigenfrequencies for the nontrivial chain. The gray shaded areas and the red boxes denote the two complete band gaps and the in-band edge states, respectively. (d) Out-of-plane displacement of the edge modes at 2676 Hz. S (A) indicates the edge mode profile is symmetric (antisymmetric) about the dotted central line.

between the two band diagrams indicates that the tight binding Hamiltonian matrices provide a satisfactory description of the elastic lattice model. The value of  $\delta f$  can be fine-tuned to zero, provided that the cross-sectional area of linking beams is neglectable as compared to that of the plate edge [43].

The topological properties of the non-Hermitian trimerized lattice can be identified by the general Zak phases [16,44,45] of the energy bands, which take the form of

$$\theta_{mn}^{\text{zak}} = i \int_{-\pi/a}^{\pi/a} \langle \xi_{m,k}^R | \partial_k | \xi_{n,k}^L \rangle dk, \quad (2)$$

where  $\xi_{m,k}^R$  and  $\xi_{n,k}^L$  are the biorthogonalized right and left eigenvectors of  $H(k)$  that satisfy  $\langle \xi_{n,k}^L | \xi_{m,k}^R \rangle = \delta_{mn}$ .  $m, n = 1, 2, 3$  represent the three energy bands, and  $k$  is the corresponding wave number. The general Zak phases accumulated from  $-\pi/a$  to  $\pi/a$  in the BZ are numerically determined to be  $\pi, 0, \pi$  for the first, second, and third band in Fig. 1(d), respectively, indicating the topologically nontrivial properties of the configuration shown in Fig. 1(b).

To examine the non-Hermiticity-controlled topological properties, we consider a finite-sized lattice with five nontrivial unit cells [Fig. 2(a)] fixed via partial plates at both ends [7,28,43]. The complex eigenfrequencies for the chain based on simulation are plotted in Figs. 2(b) and 2(c) (see Fig. S2 in the Supplemental Material [43] for the TBM results). Two band gaps (gray shaded areas) are observed as expected, which are consistent with the band diagram in Fig. 1(d). Interestingly, among the seven eigenmodes between the two band gaps, there are two topological edge modes [marked with the

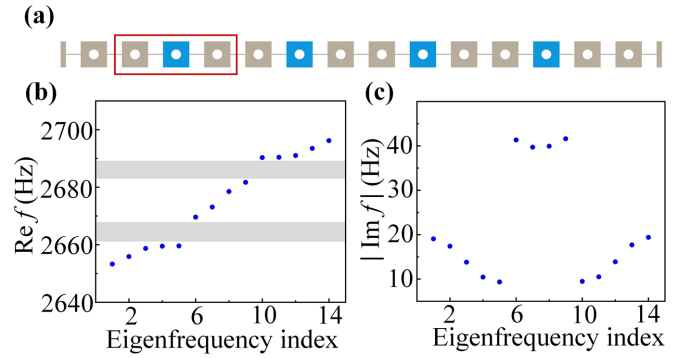


FIG. 3. Eigenfrequencies of a trimerized lattice with one defect at each end (14 sites in total). (a) Schematic of the chain with defects. The red box indicates the trimerized nontrivial unit cell. The intrinsic material damping of the whole structure is considered, while the additional damping is only added to the sites colored in blue. Simulated real parts (b) and imaginary parts (c) of the complex eigenfrequencies for the chain. The gray shaded areas denote the two complete band gaps.

red rectangle in Figs. 2(b) and 2(c)] as shown in Fig. 2(d). This is distinct from its Hermitian counterparts [43], in which the edge modes appear in the band gaps. Although these non-Hermiticity-induced edge modes lie inside the continuous spectrum, the mode energy remains perfectly confined to both ends [Fig. 2(d)] with robustness against random coupling strength disorders [43], similar to the so-called topological BICs [43].

We observe that the middle five bulk modes between the two complete band gaps possess relatively higher imaginary parts of about 40 Hz [Fig. 2(c)], implying a stronger energy dissipation. This is due to the fact that the mode shapes of the middle bulk modes exhibit large displacements on the part or all of the five plates with AD [*viz.* the plates highlighted in blue in Fig. 2(a)]. In contrast, the majority of elastic energy of the edge states is noted to be trapped in the two edge plates with only intrinsic damping (ID), as shown in Fig. 2(d), which explains the reason that edge states possess relatively lower imaginary parts (around 16 Hz).

Moreover, the existence of the edge states can be flexibly tuned by altering the boundary configurations. By way of illustration, for a chain composed of four nontrivial unit cells and one additional defect at each end [Fig. 3(a)], the edge states disappear in the eigenfrequencies spectra, as observed in Figs. 3(b) and 3(c) [see Fig. S2 in [43] for the TBM results], which are fairly distinct from the spectra of the nontrivial lattice without any defect, Figs. 2(b) and 2(c). In this case, there are four middle bulk modes with relatively higher imaginary parts, as the chain has four additional damped sites highlighted in blue.

### III. EXPERIMENTAL VALIDATION

We validate the above theoretical results and findings via experiment. In the experiment, a plate with AD treatment can be achieved by attaching a constrained damping layer on the square plate to introduce energy dissipation, as depicted in Fig. 4(a). This composite plate is composed of three layers: the constraint layer of reflective tin foil (silver layer), the

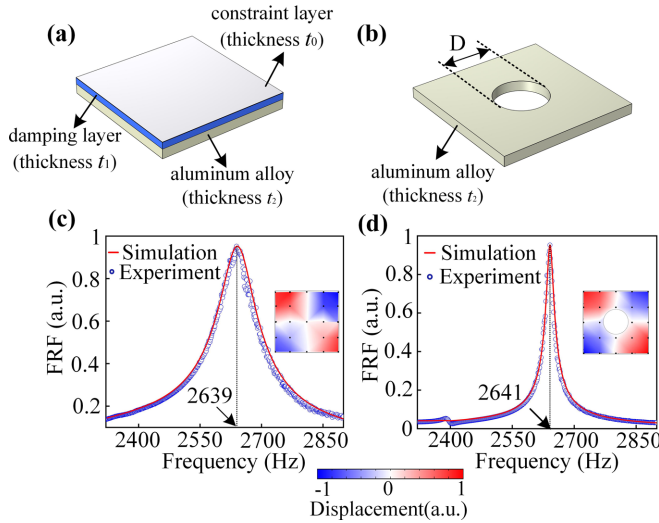


FIG. 4. Forced responses of the plates with and without the constrained damping layer. (a) Schematic of the composite plate with constrained damping layer. The plate contains three layers from top to bottom: the tin foil constraint layer (silver), the rubber damping layer (blue), and the aluminum alloy host plate (yellowish). (b) Schematic of the aluminum alloy plate with a circular through hole with diameter  $D = 15$  mm. (c), (d) FRF spectra for the single plate illustrated in (a) and (b). The blue circles are the measured results, and the red solid lines present the simulated results. The insets are the measured mode profiles at 2640 Hz.

damping layer of butyl rubber (blue layer), and the aluminum alloy plate (host plate with low intrinsic material damping, yellowish layer), from the top down, with the thicknesses of  $t_0 = 0.05$  mm,  $t_1 = 1.00$  mm, and  $t_2 = 1.46$  mm, respectively. The ultrathin reflective tin foil can not only provide a highly reflective surface for receiving vibration signals by laser vibrometer, but also increase the effective damping of the composite plate because the vibration energy is mainly attenuated by the shear deformation [46].

To obtain the frequency response function (FRF) of an individual composite plate illustrated in Fig. 4(a), the plate is suspended by a string to mimic free boundary conditions. As depicted by the blue circles in Fig. 4(c), the resonant peak is observed in the spectrum at 2639 Hz with a quality factor of  $\sim 27$ . Without the constrained damping layer, the resonant peak of the bare plate shifts to a higher frequency of 2922 Hz with a sharper shape [43], which suggests that the damping-layer treatment results in not only increased energy dissipation but also an added mass. To minimize such unwanted change in resonant frequency, the bare plate is perforated with a circular through hole (the diameter is 15 mm) at the center [Fig. 4(b)]. As a result, the measured FRF spectrum, as given in Fig. 4(d), shows a narrower resonant peak (the quality factor is  $\sim 112$ ) around 2641 Hz, which is tuned close to the original resonant frequency. The numerically calculated FRF spectra were then fitted to the experimental data to retrieve the complex Young moduli used in the above numerical simulation from Fig. 1 to Fig. 3. It turns out that the Young moduli are set to be  $E_1 = 68.9 (1 + 0.04i)$  GPa and  $E_2 = 68.9 (1 + 0.007i)$  GPa for the plate with and without the constrained damping layer, respectively.

In addition, the mode shapes of these two plates at 2640 Hz are measured and plotted in the insets of Figs. 4(c) and 4(d), respectively (the data points measured for the interpolation are indicated by the black dots in the insets). It can be seen that in spite of the constrained damping layer, the measured mode profiles still match well with the numerical results in Fig. 2(d).

With appropriately tailored damping parameters, we examine the topological properties of the 1D finite-sized lattice chains. An experimental sample, composed of 15 coupled plates without any defects, is shown in Fig. 5(a), corresponding to the chain in Fig. 2(a), and the other sample has two defects, each at one end [14 coupled plates in Fig. 5(d)], corresponding to the chain in Fig. 3(a). In these two samples, the constrained damping layers are attached on the middle plates of all the trimerized nontrivial unit cells to supply the needed non-Hermiticity.

During all measurements, the shaker with a force transducer was placed at the corner of the bulk plate marked as “4” in Figs. 5(a) and 5(d) to generate the excitation. For the sample in Fig. 5(a), the FRF curves were measured at the seventh, eighth, and first plates to respectively evaluate the bulk spectrum at the plate with ID [blue curve in Fig. 5(b)], the bulk spectrum at the plate with AD [green curve in Fig. 5(b)], and the edge spectrum [red curve in Fig. 5(b)]. Similarly, for the other sample with defects at both ends in Fig. 5(d), the seventh, ninth, and first plates were selected as the measured positions to observe the forced responses of the bulk plate with ID [blue curve in Fig. 5(e)], the bulk plate with AD [green curve in Fig. 5(e)], and the edge plate [red curve in Fig. 5(e)], respectively. More detailed information of the numerical simulation and experimental setup is presented in [43].

As depicted by the blue curve in Fig. 5(b), two dominant resonant peaks can be observed in the bulk spectrum, corresponding to the upper and lower bulk states with smaller imaginary parts [the 1st to 4th and 12th to 15th eigenfrequencies in Figs. 2(b) and 2(c)]. The green curve in Fig. 5(b) [enlarged in Fig. 5(c)] shows three resonant peaks, in which the extra one corresponds to the middle bulk bands with larger imaginary parts [the 5th, 6th, 9th, and 11th eigenfrequencies in Figs. 2(b) and 2(c)]. Different from the two bulk spectra, the edge spectrum [red curve in Fig. 5(b)] only exhibits one peak at the frequency of 2676 Hz, which signifies the existence of edge states as predicted in simulation [the seventh and eighth eigenfrequencies in Figs. 2(b) and 2(c)]. This resonant peak coincides with the middle resonant peak of the bulk spectrum at 2676 Hz [green curve in Fig. 5(b)], indicating that the topological edge states are embedded in the bulk band and coexist with the bulk resonant states. As a comparison, for the other sample with two defects, no essential difference can be observed between the blue bulk spectrum and the red edge spectrum in Fig. 5(e), as a result of the absence of the topological edge states due to the defects at the lattice boundaries. The bulk spectrum in Fig. 5(f) also highlights three separated peaks, consistent with that in Fig. 5(c).

#### IV. CONCLUSION

In conclusion, we have numerically and experimentally demonstrated the topological edge states in the continuum caused exclusively by the non-Hermiticity in a trimerized



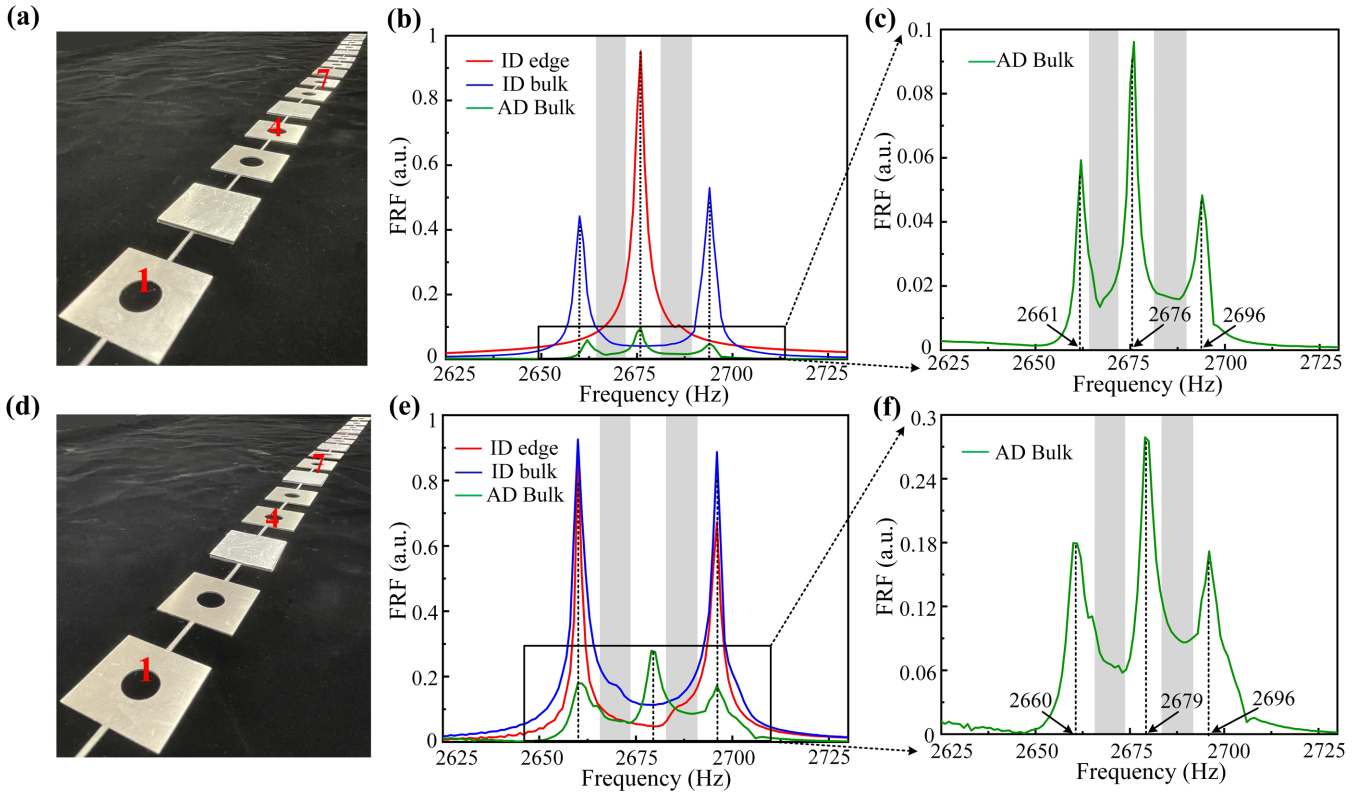


FIG. 5. Measured forced responses of the 1D finite-sized lattice chains. (a) Photo of the sample without defects. (b) Measured FRF spectra of the chain in (a). (c) Enlarged view of the green curve in (b). (d) Photo of the sample with defects at both ends. (e) Measured FRF spectra of the chain in (d). (f) Enlarged view of the green curve in (e). The red, blue, and green curves are the measured responses at the first, seventh, and eighth plates from the left end, corresponding to the edge spectrum, the bulk spectrum at the plate with intrinsic damping (ID), and the bulk spectrum at the plate with additional damping (AD) respectively. The gray shaded areas denote the complete band-gap regions.

elastic lattice. We considered two types of finite-sized trimerized chain assemblies, with and without defects at the chain ends, and showed that the in-band topological edge modes are sensitive to the boundary configurations. The boundary defects can thus serve as a switch to tune the existence of the edge states. Our findings not only provide a versatile platform to experimentally produce and manipulate topological states merely with non-Hermitian modulations, but also offer a simple and flexible approach to realizing topological BICs, which may stimulate more explorations about the rich interplay between topology and BICs, such as higher-order non-Hermitian topological states in the continuum. Moreover, since the non-Hermiticity-induced in-band topological modes lifts the requirements of band gaps, the design

flexibility for topological materials is increased. The observed non-Hermitian in-band topological modes are applicable and can be extended to various platforms in different dimensions, such as the electric circuit with negative and positive resistors [22,47], weakly coupled arrays of optical waveguides [48–50] and acoustic systems where the non-Hermitian tight binding Hamiltonian can be satisfied [43,51,52].

## ACKNOWLEDGMENTS

This work was supported by the National Natural Science Foundation of China (Grant No. 12104383) and Research Grants Council of the Hong Kong Special Administrative Region, China (Grants No. 15205219 and No. AoE/P-502/20).

- [1] X.-L. Qi and S.-C. Zhang, *Rev. Mod. Phys.* **83**, 1057 (2011).
- [2] M. Z. Hasan and C. L. Kane, *Rev. Mod. Phys.* **82**, 3045 (2010).
- [3] G. Ma, M. Xiao, and C. T. Chan, *Nat. Rev. Phys.* **1**, 281 (2019).
- [4] L. Xin, Y. Siyuan, L. Harry, L. Minghui, and C. Yanfeng, *Curr. Opin. Solid State Mater. Sci.* **24**, 100853 (2020).
- [5] T. Ozawa, H. M. Price, A. Amo, N. Goldman, M. Hafezi, L. Lu, R. C. Mikael, D. Schuster, J. Simon, O. Zilberberg, and I. Carusotto, *Rev. Mod. Phys.* **91**, 015006 (2019).
- [6] W. A. Benalcazar, B. A. Bernevig, and T. L. Hughes, *Science* **357**, 61 (2017).
- [7] M. Serra-Garcia, V. Peri, R. Susstrunk, O. R. Bilal, T. Larsen, L. G. Villanueva, and S. D. Huber, *Nature (London)* **555**, 342 (2018).
- [8] Y. Qi, C. Qiu, M. Xiao, H. He, M. Ke, and Z. Liu, *Phys. Rev. Lett.* **124**, 206601 (2020).
- [9] Z. Yang, F. Gao, and B. Zhang, *Sci. Rep.* **6**, 29202 (2016).

- [10] S. Mittal, V. V. Orre, G. Zhu, M. A. Gorlach, A. Poddubny, and M. Hafezi, *Nat. Photonics* **13**, 692 (2019).
- [11] G. M. Graf and M. Porta, *Commun. Math. Phys.* **324**, 851 (2013).
- [12] H.-X. Wang, G.-Y. Guo, and J.-H. Jiang, *New J. Phys.* **21**, 093029 (2019).
- [13] Y. Ashida, Z. Gong, and M. Ueda, *Adv. Phys.* **69**, 249 (2021).
- [14] E. J. Bergholtz, J. C. Budich, and F. K. Kunst, *Rev. Mod. Phys.* **93**, 015005 (2021).
- [15] Z. Gu, H. Gao, P.-C. Cao, T. Liu, X.-F. Zhu, and J. Zhu, *Phys. Rev. Appl.* **16**, 057001 (2021).
- [16] X. W. Luo and C. Zhang, *Phys. Rev. Lett.* **123**, 073601 (2019).
- [17] K. Takata and M. Notomi, *Phys. Rev. Lett.* **121**, 213902 (2018).
- [18] H. C. Wu, L. Jin, and Z. Song, *Phys. Rev. B* **103**, 235110 (2021).
- [19] S. Yao and Z. Wang, *Phys. Rev. Lett.* **121**, 086803 (2018).
- [20] C. Yuce and H. Ramezani, *Phys. Rev. A* **100**, 032102 (2019).
- [21] X. Zhu, H. Wang, S. K. Gupta, H. Zhang, B. Xie, M. Lu, and Y. Chen, *Phys. Rev. Res.* **2**, 013280 (2020).
- [22] S. Liu, S. Ma, C. Yang, L. Zhang, W. Gao, Y. J. Xiang, T. J. Cui, and S. Zhang, *Phys. Rev. Appl.* **13**, 014047 (2020).
- [23] W. Song, W. Sun, C. Chen, Q. Song, S. Xiao, S. Zhu, and T. Li, *Phys. Rev. Lett.* **123**, 165701 (2019).
- [24] J. M. Zeuner, M. C. Rechtsman, Y. Plotnik, Y. Lumer, S. Nolte, M. S. Rudner, M. Segev, and A. Szameit, *Phys. Rev. Lett.* **115**, 040402 (2015).
- [25] H. Gao, H. Xue, Z. Gu, T. Liu, J. Zhu, and B. Zhang, *Nat. Commun.* **12**, 1888 (2021).
- [26] H. Gao, H. Xue, Q. Wang, Z. Gu, T. Liu, J. Zhu, and B. Zhang, *Phys. Rev. B* **101**, 180303(R) (2020).
- [27] X. Zhang, Y. Tian, J.-H. Jiang, M.-H. Lu, and Y.-F. Chen, *Nat. Commun.* **12**, 5377 (2021).
- [28] H. Fan, H. Gao, S. An, Z. Gu, S. Liang, Y. Zheng, and T. Liu, *Mech. Syst. Signal Process.* **169**, 108774 (2022).
- [29] C. W. Hsu, B. Zhen, J. Lee, S. L. Chua, S. G. Johnson, J. D. Joannopoulos, and M. Soljacic, *Nature (London)* **499**, 188 (2013).
- [30] S. Vaidya, W. A. Benalcazar, A. Cerjan, and M. C. Rechtsman, *Phys. Rev. Lett.* **127**, 023605 (2021).
- [31] B. Zhen, C. W. Hsu, L. Lu, A. D. Stone, and M. Soljacic, *Phys. Rev. Lett.* **113**, 257401 (2014).
- [32] C. W. Hsu, B. Zhen, A. D. Stone, J. D. Joannopoulos, and M. Soljačić, *Nat. Rev. Mater.* **1**, 16048 (2016).
- [33] B. J. Yang, M. Saeed Bahramy, and N. Nagaosa, *Nat. Commun.* **4**, 1524 (2013).
- [34] Y. X. Xiao, G. Ma, Z. Q. Zhang, and C. T. Chan, *Phys. Rev. Lett.* **118**, 166803 (2017).
- [35] Z.-G. Chen, C. Xu, R. Al Jahdali, J. Mei, and Y. Wu, *Phys. Rev. B* **100**, 075120 (2019).
- [36] W. A. Benalcazar and A. Cerjan, *Phys. Rev. B* **101**, 161116(R) (2020).
- [37] Z.-G. Chen, L. Wang, G. Zhang, and G. Ma, *Phys. Rev. Appl.* **14**, 024023 (2020).
- [38] A. Cerjan, M. Jurgensen, W. A. Benalcazar, S. Mukherjee, and M. C. Rechtsman, *Phys. Rev. Lett.* **125**, 213901 (2020).
- [39] Y. Wang, B. Y. Xie, Y. H. Lu, Y. J. Chang, H. F. Wang, J. Gao, Z. Q. Jiao, Z. Feng, X. Y. Xu, F. Mei *et al.*, *Light Sci. Appl.* **10**, 173 (2021).
- [40] L. Jin, *Phys. Rev. A* **96**, 032103 (2017).
- [41] F. Ruzicka, *Int. J. Theor. Phys.* **54**, 4154 (2015).
- [42] B. Zhu, R. Lü, and S. Chen, *Phys. Rev. A* **89**, 062102 (2014).
- [43] See Supplemental Material at <http://link.aps.org/supplemental/10.1103/PhysRevB.106.L180302> for more discussion of the adjustment of the frequency deviation, the eigenfrequency evolution, the Hermitian case for a trimerized lattice, the robustness of the non-Hermitian edge states, the hybridization of the in-band edge states with the continuum, the boundary treatments, the acoustic counterpart of the topological bound states in the continuum, and the details for simulation and experiment, which includes Refs. [53–57].
- [44] K. Ding, Z. Q. Zhang, and C. T. Chan, *Phys. Rev. B* **92**, 235310 (2015).
- [45] F. K. Kunst, E. Edvardsson, J. C. Budich, and E. J. Bergholtz, *Phys. Rev. Lett.* **121**, 026808 (2018).
- [46] L. Cao, Z. Yang, Y. Xu, S.-W. Fan, Y. Zhu, Z. Chen, Y. Li, and B. Assouar, *J. Mech. Phys. Solids* **143**, 104052 (2020).
- [47] T. Hofmann, T. Helbig, C. H. Lee, M. Greiter, and R. Thomale, *Phys. Rev. Lett.* **122**, 247702 (2019).
- [48] H. Zhao, X. Qiao, T. Wu, B. Midya, S. Longhi, and L. Feng, *Science* **365**, 1163 (2019).
- [49] Y. Plotnik, O. Peleg, F. Dreisow, M. Heinrich, S. Nolte, A. Szameit, and M. Segev, *Phys. Rev. Lett.* **107**, 183901 (2011).
- [50] S. Mukherjee, A. Spracklen, D. Choudhury, N. Goldman, P. Ohberg, E. Andersson, and R. R. Thomson, *Phys. Rev. Lett.* **114**, 245504 (2015).
- [51] K. Ding, G. Ma, M. Xiao, Z. Q. Zhang, and C. T. Chan, *Phys. Rev. X* **6**, 021007 (2016).
- [52] W. Tang, X. Jiang, K. Ding, Y.-X. Xiao, Z.-Q. Zhang, C. T. Chan, and G. Ma, *Science* **370**, 1077 (2020).
- [53] C. Poli, M. Bellec, U. Kuhl, F. Mortessagne, and H. Schomerus, *Nat. Commun.* **6**, 6710 (2015).
- [54] S. Zheng, B. Xia, X. Man, L. Tong, J. Jiao, G. Duan, and D. Yu, *Phys. Rev. B* **102**, 104113 (2020).
- [55] C. L. Kane and T. C. Lubensky, *Nat. Phys.* **10**, 39 (2013).
- [56] F. Zangeneh-Nejad and R. Fleury, *Nat. Commun.* **10**, 2058 (2019).
- [57] K. H. Matlack, M. Serra-Garcia, A. Palermo, S. D. Huber, and C. Daraio, *Nat. Mater.* **17**, 323 (2018).